

Transmission spectroscopy of WASP-7 b with UVES [★]

Detection of Na I D₂ and tentative D₁ line absorption

Hossein Rahmati¹, Stefan Czesla², Sara Khalafinejad³, and Paul Mollière⁴

¹ Department of physics, Bu-Ali Sina University, Hamedan 65178, Iran
e-mail: h.rahmati@alumni.basu.ac.ir

² Thüringer Landessternwarte Tautenburg, Sternwarte 5, D-07778 Tautenburg, Germany

³ Landessternwarte, Zentrum für Astronomie der Universität Heidelberg, Königstuhl 12, 69117 Heidelberg, Germany

⁴ Max-Planck-Institut für Astronomie, Königstuhl 17, 69117 Heidelberg, Germany

October 26, 2022

ABSTRACT

Context. Transmission spectroscopy is a prime technique to study the chemical composition and structure of exoplanetary atmospheres. Strong excess absorption signals have been detected in the optical Na I D_{1,2} Fraunhofer lines during transits of hot Jupiters, which are attributed to the planetary atmospheres and allow us to constrain their structure.

Aims. We study the atmosphere of WASP-7 b by means of high-resolution transit spectroscopy in the sodium lines.

Methods. We analyzed a spectral transit time series of 89 high-resolution spectra of the hot Jupiter WASP-7 b that was observed using the Ultraviolet and Visual Echelle Spectrograph (UVES). We used the telluric lines for an accurate alignment of the spectra and carried out a telluric correction with `molecfit`. Stellar magnetic activity was monitored by investigating chromospheric lines such as the Ca II H and K, and hydrogen H α lines. Finally, we obtained transmission spectra and light curves for various lines.

Results. The star shows no identifiable flares and, if any, marginal changes in activity during our observing run. The sodium transmission spectra and corresponding light curves clearly show signs of the Rossiter-McLaughlin (RM) effect and the stellar center-to-limb variation (CLV) that we modeled using synthetic spectra. A statistically significant, narrow absorption feature with a line contrast of $0.50 \pm 0.06\%$ (at $\sim 8.3\sigma$ level) and a full width at half maximum (FWHM) of $0.13 \pm 0.02 \text{ \AA}$ is detected at the location of the Na I D₂ line. For the Na I D₁ line signal, we derived a line contrast of $0.13 \pm 0.04\%$ (at $\sim 3.2\sigma$ level), which we consider a tentative detection. In addition, we provide upper limits for absorption by the hydrogen Balmer lines (H α , H β , and H γ), K I $\lambda 7699 \text{ \AA}$, Ca II H and K, and infra-red triplet (IRT) lines.

Key words. Planetary Systems – Planets and satellites: atmospheres, individual: WASP-7 – Techniques: spectroscopic – Methods: observational

1. Introduction

To date, more than 5000 exoplanets have been discovered with a wide variety of masses and orbital configurations. The observed diversity raises questions regarding planetary formation, evolution, and the state of the planetary atmospheres. The latter, in particular, holds the promise to evaluate their potential to host life. Many of the known exoplanets transit their host stars. This special orbit configuration enables the use of transmission spectroscopy to study their atmospheres, which has proved to be a highly successful technique. During the transit, a fraction of the stellar light passes through the atmosphere, which leaves its footprint on it in the form of absorption by atomic and molecular species. The study of this light is the subject of transmission spectroscopy.

Hot Jupiters, which are gaseous giant planets orbiting their host stars at close proximity, are promising targets for transmission spectroscopy as their atmospheres can cover a particularly large fraction of the disks of their host star. Hot and ultra-hot Jupiters have equilibrium temperatures of $\sim 1500 \text{ K}$ and higher than 2000 K , respectively (Glidic et al. 2022). The equilibrium

temperature of a planet can be obtained using Eq. (1) by Méndez & Rivera-Valentín (2017) :

$$T_{eq} = T_{\star} \sqrt{\frac{R_{\star}}{2d}} \left(\frac{1-A}{\beta\epsilon} \right)^{\frac{1}{4}}, \quad (1)$$

where T_{\star} is the effective temperature of the star, d is the distance of the planet from the star, A is the planetary albedo, and ϵ is the broadband thermal emissivity ($\epsilon \approx 1$). The parameter β is the fraction of the planetary surface that re-radiates the absorbed flux, which is equal to one and 0.5 for quick rotators and tidally locked planets without an atmosphere, respectively (Kaltenegger & Sasselov 2011).

In fact, pronounced absorption signatures of Na I and other alkali metals were predicted to show in optical transmission spectra by early models (Seager & Sasselov 2000; Brown 2001) and, indeed, the first detection of Na I in-transit excess absorption in the atmosphere of HD 209458 b soon followed (Charbonneau et al. 2002), though it has not remained unchallenged (Casasayas-Barris et al. 2020, 2021). The first reports of ground-based detections of in-transit excess absorption in the Na I D lines were provided by Redfield et al. (2008) and Snellen et al. (2008), who studied the atmospheres of HD 189733 b and

[★] Based on observations collected at the European Southern Observatory under ESO programme ID 091.C-0632(A) (PI: F. Pfeifer).

Table 1. Orbital and physical parameters of the WASP-7 system.

Parameter	Symbol	Value	Ref.
Stellar parameters			
Stellar brightness	V [mag]	9.51	1
Stellar mass	M_* [M_\odot]	1.285 ± 0.063	2
Stellar radius	R_* [R_\odot]	1.466 ± 0.094	2
Stellar effective temperature	T_{eff} [K]	6400 ± 100	2
Projected stellar rotation speed	$v \sin i$ [km s^{-1}]	14 ± 2	3
Metallicity	[Fe/H]	0.0 ± 0.1	2
Planet parameters			
Planet Mass	M_p [M_{Jup}]	$1.083^{+0.093}_{-0.088}$	2
Planet Radius	R_p [R_{Jup}]	1.363 ± 0.093	2
Planet surface gravity	$\log g_p$ [cgs]	$3.159^{+0.071}_{-0.068}$	2
Equilibrium temperature	T_{eq} [K]	1530 ± 45	4
Transit parameters			
Orbital Period	P [d]	$4.9546416 \pm 3.5 \times 10^{-6}$	3
Mid-transit	T_0 [BJD _{TDB} -2,400,000]	55446.635 ± 0.0003	3
Transit duration	T_{14} [h]	$4.12^{+0.09}_{-0.06}$	3
Ingress duration	T_{12} [min]	27^{+6}_{-9}	3
System parameters			
Orbital inclination	i [deg]	87.03 ± 0.93	5
Semimajor axis	a [AU]	$0.06188^{+0.00098}_{-0.001}$	2
Stellar velocity semi-amplitude	K_* [m s^{-1}]	$109.4^{+8.3}_{-8.1}$	2
Systemic velocity	γ [km s^{-1}]	-29.35 ± 0.53	6
Projected obliquity	λ [deg]	86 ± 6	3

References. (1) [Hellier et al. \(2009\)](#); (2) [Bonomo et al. \(2017\)](#); (3) [Albrecht et al. \(2012\)](#); (4) [Southworth \(2012\)](#); (5) [Southworth et al. \(2011\)](#); (6) [Gaia Collaboration et al. \(2018\)](#).

HD 209458 b, respectively. High-resolution transmission spectroscopy has allowed the individual Na I transmission line profiles to be resolved (e.g., [Wytttenbach et al. 2015, 2017](#); [Seidel et al. 2019](#)), which makes the Na I signatures a particularly powerful probe to constrain the upper atmosphere ([Wytttenbach et al. 2015](#); [Nikolov et al. 2018](#)).

The hot Jupiter, WASP-7 b, was discovered using the transit method by [Hellier et al. \(2009\)](#). The planet orbits an F-type star, HD 197286, with an orbital period of 4.954 d. The main properties of the system are summarized in Table 1. Notably, the orbit of WASP-7 b denotes an obliquity of $86^\circ \pm 6^\circ$, indicating an almost polar orbit ([Albrecht et al. 2012](#)). This special configuration makes the WASP-7 system a promising candidate to study differential rotation via the planetary transit ([Serrano et al. 2020](#)).

In this paper, we present our analysis of a high-resolution spectral transit time series of WASP-7 b, obtained with the Ultraviolet and Visual Echelle Spectrograph (UVES) at the Very Large Telescope (VLT). The structure of this paper is as follows. In Sect. 2, we present the observations and data reduction. In Sect. 3, we investigate the stellar activity, focus on Na I D lines, and provide upper limits of plausible absorption for other lines. Finally, we present a discussion and conclusion in Sects. 4 and 5.

2. Observations and data reduction

A high-resolution spectral time series of WASP-7 b was obtained on 31 August 2013 in the context of ESO programme 091.C-0632(A) using UVES ([Dekker et al. 2000](#)), mounted on the Kueyen telescope (UT2), which is part of the VLT. We downloaded the data from the ESO archive and carried out the data reduction using standard recipes from the UVES pipeline. In particular, the pipeline performs bias subtraction, flat fielding, and wavelength calibration. Finally, the spectra are merged into 1D science spectra. With our settings, the UVES instrument covers the wavelength range from 380 to 950 nm.

The time series comprises 89 spectra with a spectral resolution of 60 000 in the Na I regions. A total of 20 exposures were obtained before ingress; 49 during the transit and 20 after egress. The first 34 exposures, exposure 48, and exposures 79-89 have an exposure time of 300 s, while the remaining exposures have an exposure time of 200 s. In the top panel of Fig. 1, we show the evolution of airmass and seeing during the observing run. The airmass ranges between 1.03 and 1.98 during the observing run. The average seeing is 1.24 arcsec and its evolution roughly follows that of airmass. The bottom panel of Fig. 1 displays the time evolution of the signal-to-noise ratio (S/N) per spectral bin in the region of the Na lines, estimated from the data using the $\beta\sigma$ procedure ([Czesla et al. 2018](#)). The average S/N value of the spectra is about 150, starting higher at about 178 when the run

starts, after which it slightly decreases toward the end of the observing run.

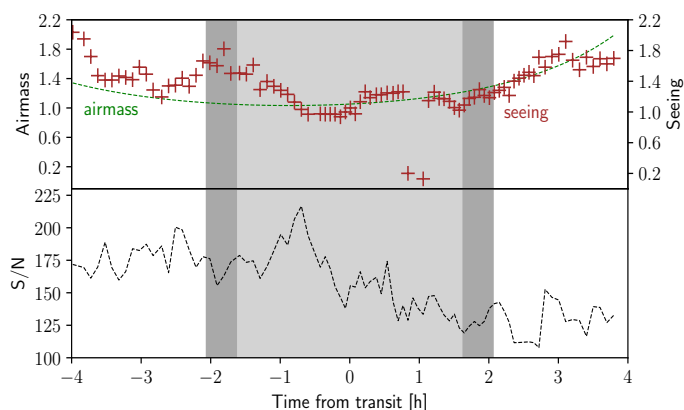


Fig. 1. Time evolution of seeing in arcsec (brown crosses, top panel), airmass (dashed green lines, top panel), and S/N in the regions of the Na doublet lines (bottom panel). Dark gray shades indicate the ranges of ingress and egress, and light shades show the range between second and third contact.

2.1. Telluric correction

Ground-based high-resolution spectra are affected by the features originating in the Earth’s atmosphere, and changes in airmass and atmospheric conditions along the line of sight cause variations in the telluric lines. We corrected the telluric lines in the Na I D, H α , K I, and Ca II infra-red triplet (IRT) line regions using the molecfit package (Smette et al. 2015; Kausch et al. 2015). The molecfit package fits a synthetic transmission spectrum of the Earth’s atmosphere to suitable sections of the observed spectrum and, subsequently, corrects the telluric contamination in the observed spectrum using the synthetic model evaluated across the entire observed range. Clearly, the regions of the Na I and H α lines are mostly affected by water lines. In the Ca II H and K line region, telluric lines remain irrelevant. As an example of our telluric correction, we show the last spectrum of our time series in the Na I D and H α regions in Fig. 2. This exposure exhibits the largest airmass and is most strongly affected by telluric absorption (Fig. 1, top panel).

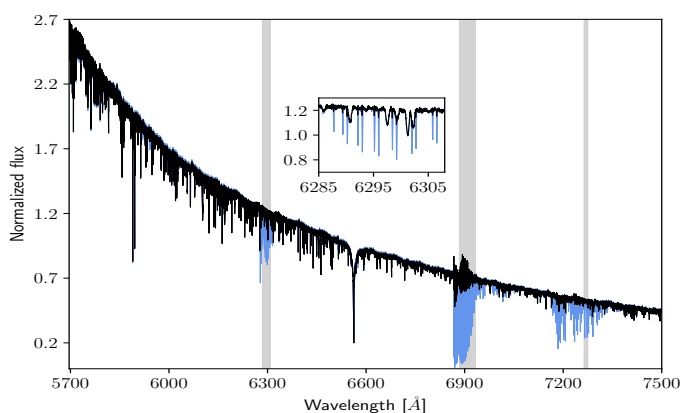


Fig. 2. Spectrum before (blue) and after (black) telluric correction. The gray shaded regions denote sections used for fitting with molecfit.

2.2. Spectral alignment

In high-resolution transmission spectroscopy, an accurate alignment of the spectra is crucial because misalignment can produce remnants in the transmission spectrum. The dispersion in UVES is known to depend on pressure and temperature (e.g., Czesla et al. 2012). Therefore, we used the wavelengths of 39 telluric lines, which provide a reference for the Earth’s system of rest, accurate to within about 25 m s^{-1} (e.g., Caccin et al. 1985; Gray & Brown 2006), to refine the alignment. In Fig. 3, we show the median shift of the telluric lines along with the evolution of the barycentric correction (BC). We also accounted for the stellar orbit velocity, which remains small, taking values between -22 and 22 m s^{-1} during the observing run. Finally, we considered a systemic shift of -29.35 km s^{-1} for the WASP-7 system (Gaia Collaboration et al. 2018). To test the accuracy of our alignment, we fit Gaussian profiles to the cores of the Na I lines after the alignment. The results are consistent with static line cores and a radial velocity (RV) standard deviation of 10 m s^{-1} .

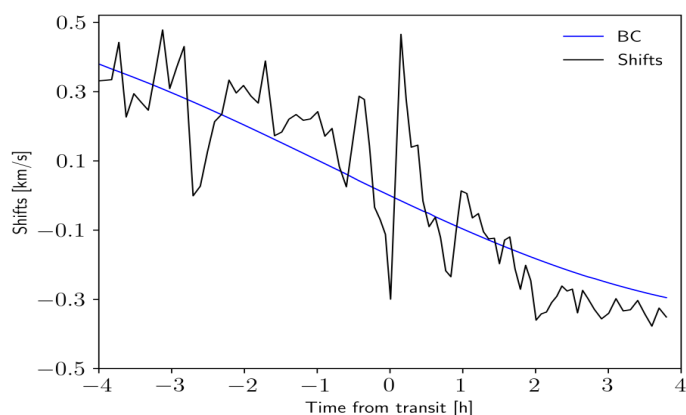


Fig. 3. Time evolution of BC and median telluric shifts used for spectral alignment.

3. Data analysis

3.1. Stellar activity

Stellar activity is a common nuisance in transmission spectroscopy. Stellar flares can produce strong spectral evolution in the cores of chromospherically sensitive lines such as the Ca II H and K lines, the corresponding infrared triplet, the H α line, and notably also the Na I D lines on a timescale of minutes to hours (e.g., Klocová et al. 2017), posing serious problems to planetary transmission spectroscopy (e.g., Barnes et al. 2016; Khalafinejad et al. 2017). In addition, stellar surface features such as starspots and plage regions can influence the transmission spectrum (e.g., Oshagh et al. 2014; Cauley et al. 2018; Salz et al. 2018).

We investigated the Ca II H and K, and H α lines to search for signs of evolution in activity, such as flaring. In particular, we integrated the flux in a 0.45 \AA wide passband centered on each of the Ca II H and K lines, and in broader reference bands on both sides (see Fig. 4, top panel), and we derived a light curve by dividing the fluxes in the integration and reference bands. A comparable analysis was carried out for the H α line (see Fig. 5). The resulting light curves, shown in the bottom panels of Figs. 4 and 5, reveal no discernible flaring activity and are consistent with a constant level of activity with, at most, marginal evolution.

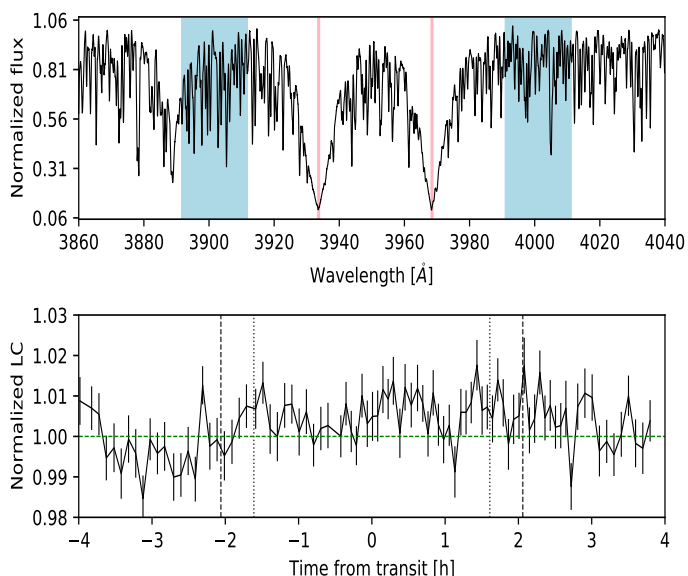


Fig. 4. Integration and reference bands in the Ca II H and K line region (top), and normalized Ca II H and K light curves. Dashed vertical lines show first and fourth contact, and the dotted vertical lines show second and third contact.

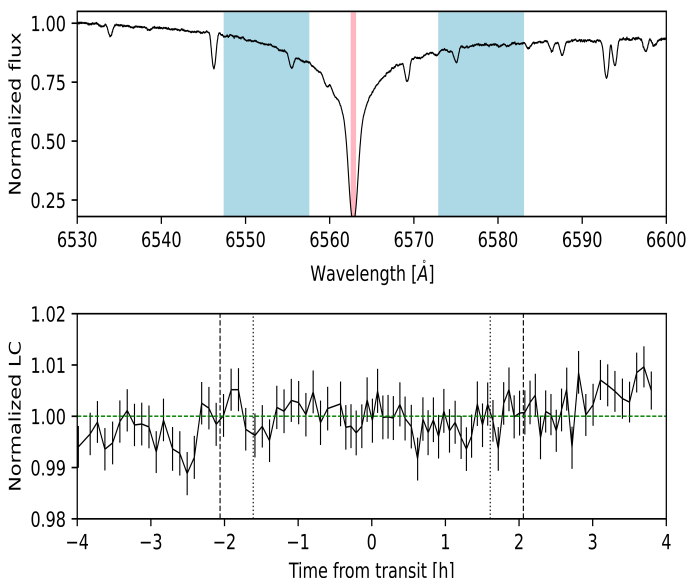


Fig. 5. Integration and reference bands in the H α line region (top) and the normalized H α light curve. Dashed vertical lines indicate first and fourth contact, and the dotted vertical lines indicate second and third contact.

3.2. Master and residual spectra

In a first step, we obtained separate weighted pre- and post-transit master spectra by averaging the respective spectra of the time series. The ratio of these spectra around the Na I lines is displayed in Fig. 6. No significant relics can be distinguished at the wavelengths of the Na I line cores, which might indicate potential shortcomings of our alignment (Sect. 2.2) or traces of activity. We then proceeded to obtain a weighted master out-of-transit spectrum (OOT master) by averaging all out-of-transit spectra and dividing all spectra of the time series by this OOT master to produce the residual spectra.

The residual spectra can be used to study spectral changes with respect to the OOT master. Such changes may be brought

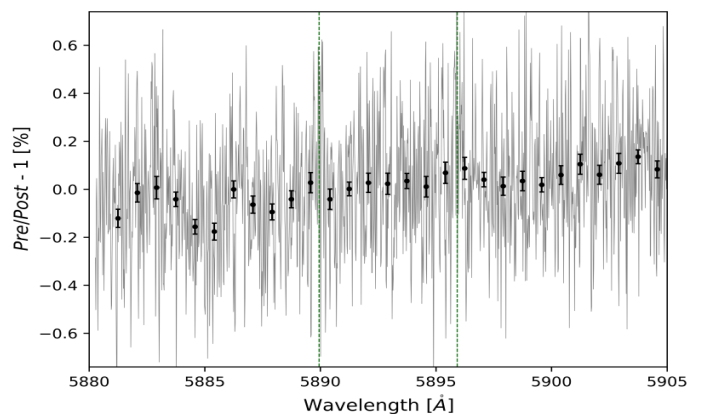


Fig. 6. Ratio of pre- and post-transit master spectra (light gray) along with binned spectral ratio (black circles). Dashed vertical green lines indicate the centers of Na I lines.

about by absorption in the planetary atmosphere, as well as variability in the stellar lines and statistical effects. The planetary atmospheric signal, in particular, is expected to move through the stellar line along with RV caused by the planetary orbital motion. Therefore, to study the planetary signal, we produced residual spectra by shifting all in-transit residual spectra into the planetary frame:

$$R = \frac{F_{in}(\lambda)}{F'_{out}}(\lambda)|_{Planet\ RV\ shift} - 1, \quad (2)$$

where

$$F'_{out}(\lambda) = \frac{\sum F_{out} W_{S/N}(F_{out}(\lambda))}{\sum W_{S/N}(F_{out}(\lambda))}, \quad (3)$$

and $F'_{out}(\lambda)$ is the weighted OOT master, $F_{out}(\lambda)$ denotes the out-of-transit spectra, and $W_{S/N}(F_{out}(\lambda))$ represents the weights, which are based on the S/N of the individual out-of-transit exposures.

3.3. Center-to-limb variation and Rossiter-McLaughlin effects

The center-to-limb variation (CLV) describes the spectral variation of the stellar disk as a function of the limb angle. During the transit, the opaque planetary disk subsequently covers different sections of the rotating stellar surface. The combined action of rotational shift and CLV gives rise to pseudo-signals in the transmission spectrum, unrelated to the planetary atmosphere (e.g., Khalafinejad et al. 2017; Salz et al. 2018; Casasayas-Barris et al. 2020). Such pseudo-signals can be particularly pronounced in strong absorption lines such as the Ca II H and K or Na I lines (e.g., Czesla et al. 2015; Yan et al. 2015).

To account for the pseudo-effects in our analysis, we simulated the time series of transmission spectra resulting from the transit of the opaque planetary disk alone, following the methodology presented by Czesla et al. (2015). In particular, we used a discretized, rotating stellar surface (Vogt et al. 1987) and limb-angle resolved model spectra of the stellar disk, synthesized using the spectrum¹ program by R.O. Gray (e.g., Gray & Corbally 1994) based on Kurucz atmospheric models (e.g., Castelli & Kurucz 2003). Blocking the light from the respective surface

¹ <https://www.appstate.edu/~grayro/spectrum/spectrum.html>

elements covered by the advancing planetary disk yields the theoretical spectrum at any point in time during the transit, which is then compared with the disk-integrated stellar spectrum to assess the expected pseudo-signals. In Fig. 7, we indicate the modeled spectral time evolution caused by the CLV and the Rossiter-McLaughlin (RM) effects as a 2D heat map; the resulting light curve and transmission spectrum are shown in Figs. 8 and 10, respectively.

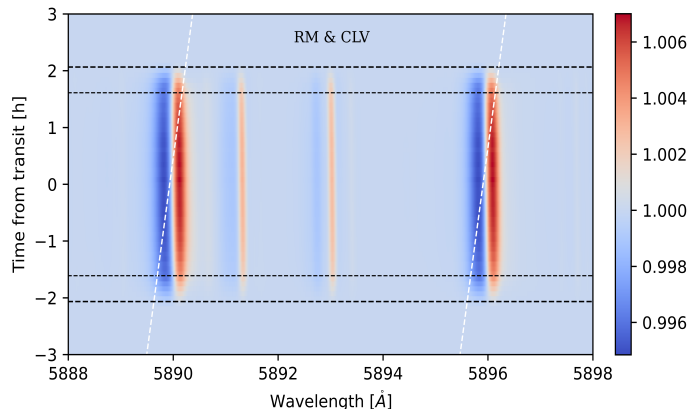


Fig. 7. 2D heat map of the modeled CLV and RM effects of WASP-7 b around the Na I D doublet denoted in the stellar rest frame. Horizontal dashed and dotted lines indicate the transit contact, and the dashed white lines show the planetary RV track.

3.4. Transmission light curves

To derive transmission light curves for the Na I D lines, we integrated the shifted residual spectra in 0.45 \AA wide passbands, centered on the nominal positions of the Na I D lines, and compared that result to the flux in suitable reference passbands within 15 \AA of the Na I D lines' center. The light curve was then normalized by the mean out-of-transit level.

In Fig. 8, we show the light curves acquired in this way for the stronger Na I D₂ line. We modeled the light curves using increasingly complex models, and show the best-fit results and the values of the Bayesian Information Criterion (BIC, Schwarz 1978) in Table 2. Uncertainties were obtained by Markov chain Monte Carlo (MCMC) sampling². We started by using a constant, c , and subsequently added a slope, s . According to the BIC, the introduction of a slope is not merited, so we dropped that component. Adding the simulated pseudo-signals caused by the CLV and RM effects to the model improved the BIC by 109.1, providing very strong evidence for the component (Kass & Raftery 1995). Finally, we included a box-like transit model, which represented in-transit absorption in the Na I D₂ line potentially attributable to the planetary atmosphere. The best-fit depth, b , of the absorption box model was $(1.7 \pm 0.25) \times 10^{-3}$ and its introduction improved the BIC by 39.1 compared to the previous model, which again provides strong evidence. In Fig. 8, we show the final model, along with its individual components in the top panel and the resulting residuals in the bottom panel.

As an additional test, we estimated the uncertainty of the depth of the box-like transit model using the jackknife method, the idea of which is to analyze the response of the fit to leaving out individual data points (e.g., Efron & Stein 1981). The resulting estimate for the depth was $(1.7 \pm 0.5) \times 10^{-3}$. The larger error

² We used the emcee (Foreman-Mackey et al. 2013) and PyAstronomy packages (Czesla et al. 2019).

Table 2. Best-fit parameters of the Na I D₂ line transmission light curve, along with 68 % credibility intervals and BIC.

	Constant
c	0.99910 ± 0.00012
BIC	466.6
Constant and slope	
c	0.99908 ± 0.00012
$s [\text{\AA}^{-1}]$	-0.0049 ± 0.007
BIC	470.6
Constant and CLV	
c	0.99919 ± 0.00012
BIC	357.5
Constant, CLV, and box	
c	1.00020 ± 0.00020
b	0.00170 ± 0.00025
BIC	318.4

estimate resulting from applying the jackknife method may indicate that the errors of the data were underestimated. Adopting the more conservative jackknife estimate, which takes into account the empirical distribution of the data, we obtained 3.4σ for the significance of the absorption component.

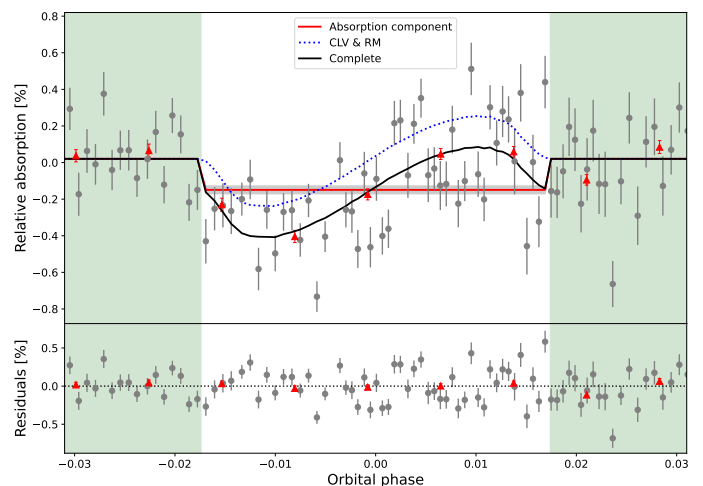


Fig. 8. Transmission light curves of WASP-7 b around the Na I D₂ line. Top panel: Observation transmission light curves (gray) and modeled transmission light curves of the RM and the CLV (dotted blue line) for the 0.45 \AA integration band centered on the Na I D₂ line. The dashed red line is the absorption component using a box model, and the gray shades denote its 1σ uncertainty. The solid black line is the best-fit combined model and the red points show binning by a factor of ten. Bottom panel: Residuals for binned and unbinned data. Green shades indicate out-of-transit time throughout.

3.5. The transmission spectrum

We obtained the transmission spectrum as the weighted average of the shifted residual spectra between the second and third contact:

$$\mathcal{R}'(\lambda) = \frac{\sum R_{\text{in}} W_{S/N}(F_{\text{in}}(\lambda))}{\sum W_{S/N}(F_{\text{in}}(\lambda))}, \quad (4)$$

where R_{in} are the in-transit residuals and $W_{S/N}(F_{\text{in}}(\lambda))$ represents the weights, which are based on the S/N of the individual exposures.

As demonstrated, for instance, by Czesla et al. (2015) and Casasayas-Barris et al. (2020), the effect of the CLV and the RM effects on the transmission spectrum can be significant. Therefore, we derived a synthetic transmission spectrum (Sect. 3.3), which exclusively shows the effect of the CLV and the RM effects and is indicated in the upper panel of Fig. 10, along with the data.

We modeled the observed transmission spectrum in the range from 5880 Å to 5905 Å using the sum of three components: (1) a linear model with a free offset (p_0) and slope (p_1) to account for possible slopes in the transmission spectrum; (2) the synthetic transmission spectrum with a free scaling parameter (s) to account for systematic differences between the true stellar spectrum and the adopted synthetic spectrum of the stellar photosphere; and (3) two Gaussian components, representing possible planetary absorption components in the Na I D₁ and D₂ lines. While the two Gaussian components were set up to show the same width and RV shift with respect to the nominal rest wavelengths of the Na I D₁ and D₂ lines, we treated their strengths as independent. The free parameters of the Gaussian model were, therefore, a common RV shift and standard deviation, and the area of the Gaussians. We then applied Powell’s method to find the maximum likelihood solution and, subsequently, carried out MCMC sampling, using uniform priors for the parameters, to find credibility intervals³. The best-fit parameters, along with their uncertainties, are given in Table 3. In Fig. 9, we indicate the time evolution of the spectral residuals in the form of a 2D heat map, and in Fig. 10, we show the observed transmission spectrum along with our best-fit model.

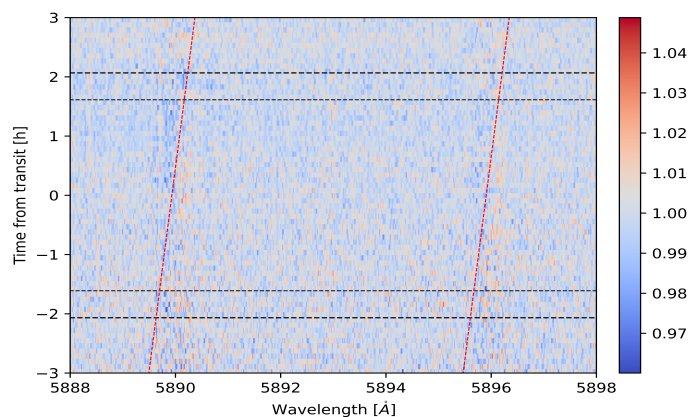


Fig. 9. 2D heat map of the transmission spectra of WASP-7 b around the Na I D doublet indicate in the stellar rest frame without considering the CLV and RM effects. Horizontal dashed and dotted lines show the transit contact and the dashed red lines denote the planetary RV track.

The transmission spectrum in Fig. 10 indicates an absorption feature at the position of the Na I D₂ line. According to our modeling, the line contrast (i.e., the depth) of the Na I D₂ component is $0.5 \pm 0.06\%$, which corresponds to an $\sim 8.3\sigma$ detection. For the Na I D₁ line, we find a best-fit contrast of $0.13 \pm 0.04\%$ and, thus, a signal at the 3.2σ level. The best-fit value of the full width at half maximum (FWHM) is $0.13 \pm 0.02\text{ Å}$, which is slightly larger than the instrumental resolution, indicating a narrow intrinsic absorption component. We find a RV shift of $0.3 \pm 0.4\text{ km s}^{-1}$ for the Gaussian components, consistent with a signal at the rest wavelength. The line shift and width are clearly driven by the D₂ line signal.

³ We used SciPy (Virtanen et al. 2020), PyAstronomy (Czesla et al. 2019), and emcee (Foreman-Mackey et al. 2013).

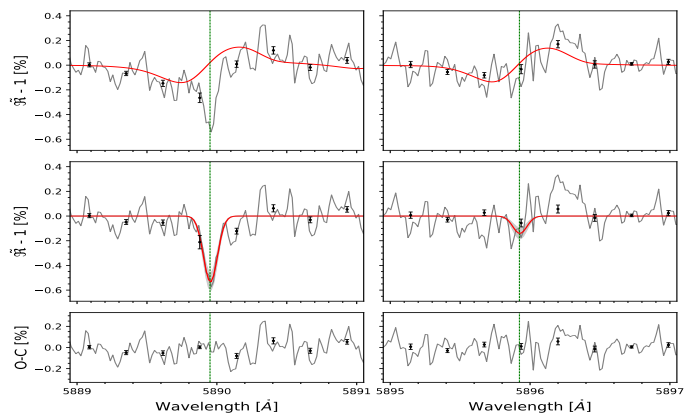


Fig. 10. Transmission spectrum of WASP-7 b around the Na I D₂ (left column) and Na I D₁ (right column) lines. Top panels: Observed transmission spectrum (gray), along with best-fit model components representing the CLV and RM effects (solid red). Middle panels: Observed transmission spectrum with the best-fit Gaussian absorption components (red), and with the model shown in the upper panels subtracted (gray). The gray shades indicate 1σ uncertainty of the best-fit model (red). Bottom panel: Residuals with respect to the best-fit model. The black data points correspond to binning by a factor of 15.

Table 3. Best-fit parameters along with 68 % credibility intervals of the transmission spectrum model. Values of the BIC for four variants of the model (see text).

Parameter	Value	Unit
p_0	0.0138 ± 0.0035	
p_1	0.0016 ± 0.0003	$[\text{Å}^{-1}]$
s	0.435 ± 0.040	
RV	0.32 ± 0.41	$[\text{km s}^{-1}]$
Contrast D ₂	0.500 ± 0.064	$[\%]$
Contrast D ₁	0.134 ± 0.043	$[\%]$
FWHM	0.135 ± 0.025	$[\text{Å}]$
Model	k	BIC
No s	6	1554.5
No Abs	3	1571.0
Only D ₂	6	1437.9
Only D ₁	6	1580.3
D ₁ and D ₂	7	1434.1

To further assess the significance of the absorption line components, we calculated the BIC for a total of four model configurations (Table 3). First, no scaling pseudo-effects was examined (No s). Second, no sodium absorption was investigated at all (No Abs). Then, absorption was only considered in the D₂ and D₁ lines individually (Only D_{1,2}). Finally, the BIC was calculated for the full model with absorption in both lines (D₁ and D₂). In Table 3, we also give the respective number of free model parameters (k). As the widths and contrasts of the Gaussians were coupled, only one additional parameter was introduced by going from a model with a single line to both absorption lines. In line with the error analysis, the BIC provides strong evidence for D₂ absorption, but not D₁ absorption.

In an attempt to improve the observed transmission spectrum, we constructed an alternative transmission spectrum by ignoring the ten spectra with the lowest S/N in the observing run, which corresponded to the post-transit exposures 70-80. We then performed the same modeling and obtained a line contrast of $0.49 \pm 0.05\%$ ($\sim 9.8\sigma$) and $0.19 \pm 0.03\%$ ($\sim 6.3\sigma$) for the Na I D₂ and D₁ lines, respectively, with a FWHM of 0.17 ± 0.02

Å. This yielded a more significant absorption feature in the Na I D₁ line.

The detection of the Na I D₂ feature is statistically significant at $\sim 8.3\sigma$ level between the second and third contact. As a cross-check, we also obtained the transmission spectra corresponding to the first and second halves of the transit individually. The Na I D₂ line contrasts in the first and second halves of the transit, acquired from a fit with line width fixed to the value given in Table 3, are $0.53 \pm 0.04\%$ and $0.49 \pm 0.08\%$, respectively. The feature is slightly more pronounced in the first-half transmission spectrum of the transit, which may be related to the better S/N during the first half. We derived an average contrast of $0.51 \pm 0.06\%$, which is consistent with the result of the Na I D₂ line contrast in Table 3.

3.6. Relation to the transmission light curve

The equivalent width (EW) of the Gaussian fit to the Na I D₂ signal is 0.69 ± 0.14 mÅ (Table 3). Therefore, the mean depth (in percent) across a band of width w (given in Å), fully comprising the signal, can be calculated as $(0.069 \pm 0.014)w^{-1}$. Adopting $w = 0.45$ Å as in Sect. 3.4, we find an average depth of $0.15 \pm 0.03\%$, which is consistent with the result of the light curve analysis.

In light of the spectral results, we also constructed a transmission light curve in a narrower 0.15 Å wide band. From the same analysis as in Sect. 3.4, we find a depth of $(0.309 \pm 0.084) \times 10^{-3}$ for the respective box model, which is in line with a narrow signal. While no scaling of the simulated pseudo-effects was indicated in the light curve analysis (Sect. 3.4), scaling does improve the fit to the transmission spectra (Table 3). We speculate that the different behavior is related to the much wider wavelength range of the transmission spectrum sensitivity considered in this analysis and the resulting change in sensitivity to the model.

3.7. Upper limits for absorption lines

We carried out the same analysis to derive the transmission spectrum of the hydrogen Balmer lines (H α , H β , and H γ), K I $\lambda 7699$ Å, Ca II H and K, and the IRT lines. No absorption feature associated with these lines was detected. We computed the standard deviation of the continuum in the regions of the lines and considered that as an upper limit for the line contrast (Table 4).

Table 4. Upper limits of lines in the transmission spectrum of WASP-7 b with UVES.

Line	Value
H α	0.13 %
H β	0.12 %
H γ	0.12 %
K I $\lambda 7699$ Å	0.10 %
Ca II H and K	0.16 %
Ca II IRT	0.11 %

4. Discussion

4.1. Comparison with the atmospheric model

To model the transmission spectrum of WASP-7 b, we used the `petitRADTRANS` (pRT) python package (Mollière et al. 2019),

which enables the calculation of transmission and emission spectra of exoplanets at low and high resolution. We adopted the line-by-line mode for the sodium lines and considered Rayleigh scattering by H₂. Collision-induced absorption was ignored because its opacity does not have a critical effect at the observed wavelength. We further adopted a solar sodium abundance, a mean molecular weight of 2.3, and an isothermal atmosphere with the equilibrium temperature given in Table 5 to set up the atmospheric model. The pressure range of the atmosphere between 100 and 10^{-12} bar was sampled with 100 layers. We checked that the setup was sufficient by calculating the transmission contribution function in the center of the line core, which showed that the contribution of lower pressure layers was negligible. Finally, we created a model transmission spectrum using the radius, temperature, and surface gravity of the planet at a reference pressure, P_0 , of 0.1 bar.

The resulting model, accounting also for instrument resolution, is shown as the red profile in Fig. 11. The model produces absorption in the Na I D₂ line. The line wings seen in the model are undetectable in our data. Approximating the modeled line by a Gaussian, we find a line contrast of 0.15 % and a FWHM of 0.14 Å. The model reproduced the observed width of the line core, but the line is weaker. The modeled Na I D₂ line strength can, for example, be increased by assuming a higher temperature or a lower mean molecular weight, effectively increasing the atmospheric scale height. Therefore, we also constructed alternative models. We increased the temperature and sodium abundance, first by 30 % (blue line in Fig. 11), and then by 50 % (green profile). The observed Na I D₂ line contrast was still not reproduced. We speculate that the assumption of hydrostatic equilibrium is violated altogether and material from a possibly escaping exosphere may contribute to the absorption, as has been proposed for some lines in other planets (Zhang et al. 2022).

All of these models considered here display similar absorption in both Na I D lines, which is hardly compatible with our observations. Moreover, for these models, the strength of the Na I D₂ line is underestimated, while that of the D₁ line is overestimated. Increasing the temperature or Na abundance increases the absorption in both lines, but not sufficiently to reproduce the Na I D₂ signal in the transmission spectrum.

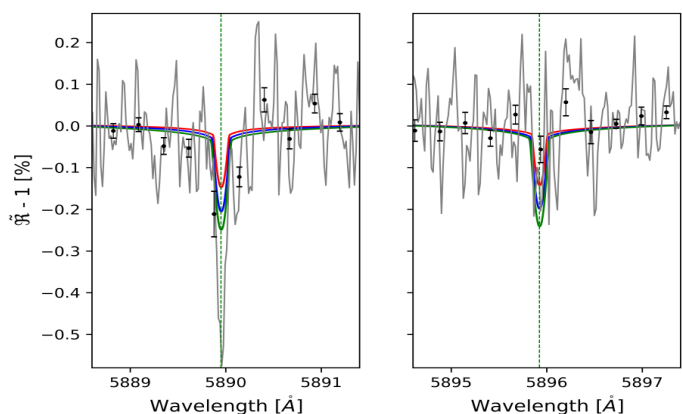


Fig. 11. Transmission spectrum of WASP-7 b (gray) around the Na I D₂ (left column) and Na I D₁ line (right column), along with atmospheric models (red, blue, and green).

4.2. Comparison with known Na I signals

In Table 5, we compare key parameters of WASP-7 b to those of other systems with previously reported detections of absorption in the Na I D lines and reported Gaussian fit parameters. In particular, we give the equilibrium temperature of the respective planet, along with an estimate of the scale height, H , calculated assuming a mean molecular weight of 2.3 for the atmosphere, and the resulting fractional area of the stellar disk, covered by the atmospheric annulus per scale height during transit:

$$\Delta A = \frac{2\pi R_p H}{\pi R_\star^2}, \quad (5)$$

where R_p and R_\star are the planetary and stellar radii, respectively. Finally, we list the line contrast and FWHM of Gaussian fits to the observed transmission signal in the Na I D lines.

In Fig. 12, we compare the fractional atmospheric coverage, ΔA , with the excess absorption as measured by the EWs of Gaussian fits to the D₂ line. Among the listed exoplanets, WASP-52 b shows the largest fractional atmospheric coverage per scale height and the largest observed EW. On the other end of the scale, MASCARA-2 b exhibits the smallest fractional coverage, as well as a narrow absorption line with a low EW. For the considered systems, larger fractional coverage tends to be correlated with stronger absorption in the Na I D₂ line core, with a value of 0.82 for Pearson's correlation coefficient. Although the low number of systems prevents a strong conclusion regarding the relation, the signal found in WASP-7 b fits well in the picture.

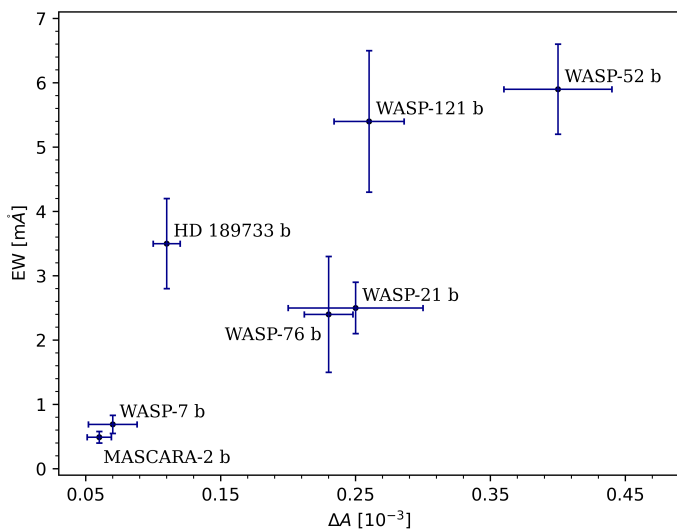


Fig. 12. Excess absorption as indicated by Gaussian fits to the Na I D₂ line as a function of fractional atmospheric coverage ΔA .

In their analysis of planetary sodium absorption in a sample of ten systems, which comprises the sample of Table 5, apart from WASP-7, Langeveld et al. (2022) point out an empirical relation between the height of the atmosphere absorbing in the Na I D₂ line center divided by the planetary radius, h_{Na} , and the quantity:

$$\xi = \left(\frac{T_{\text{eq}}}{1000 \text{ K}} \right) \times \left(\frac{g}{g_{\text{J}}} \right), \quad (6)$$

where T_{eq} is the equilibrium temperature, g is surface gravity, and g_{J} is the surface gravity of Jupiter. In Fig. 13, we use

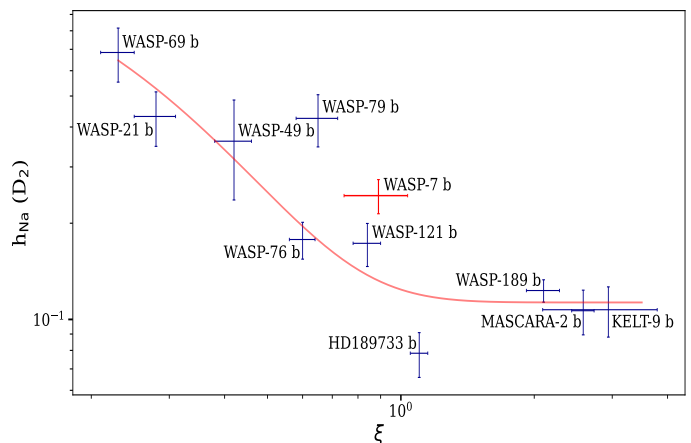


Fig. 13. Height of atmosphere absorbing in the Na I D₂ line center divided by planetary radius as a function of ξ , along with the relation fitted by Langeveld et al. (2022).

the data published by Langeveld et al. (2022), which are weight combined, along with their best-fit relation, and add the data of WASP-7. The data points associated with WASP-7 lie above the best-fit relation given by Langeveld et al. (2022), but fit reasonably well into the relation and are not outliers.

The FWHMs of the listed Na I D₂ line signals vary by a factor of about six, ranging from 0.13 Å to 0.73 Å, but, with the notable exception of the case of WASP-52 b, the widths of the Na I D₁ and D₂ lines listed in Table 5 are consistent within two standard errors, which is in line with the modeling results we obtained for WASP-7 b (Sect. 4.1). Of the cases shown in Table 5, WASP-7 b shows the lowest measurement of line width. The Na I D₂ transmission spectra of WASP-7 b and MASCARA-2 b are quite similar in width and overall strength. However, in contrast to MASCARA-2 b, where Casasayas-Barris et al. (2019) also detected a Na I D₁ line of comparable strength, we found a considerably weaker Na I D₁ line in WASP-7 b.

In their analysis, Langeveld et al. (2022) find that the ratio of contrasts of the Na I D₂ and D₁ transmission lines is consistent with one in seven systems and larger than one in three systems. Taking the values for WASP-7 b in Table 5 at face value, we obtained ratios of 3.8 ± 1.3 and 2.6 ± 0.5 with the alternative analysis, discarding the ten post-transit spectra with the lowest S/N. For comparison, the largest ratio found by Langeveld et al. (2022) is 2.6 ± 1.37 (weight-combined spectra) for WASP-69 b, which is consistent with the numbers for WASP-7 b within the standard error. In principle, an overestimation of the Na I D₂ line contrast, an underestimation of the Na I D₁ line contrast, or both, could raise the ratio.

Excluding the ten post-transit spectra with the lowest S/N, which raises the measured Na I D₁ line contrast in our analysis, may indicate that the discrepancy may at least partially be caused by properties of the data possibly related to the S/N, or brought about by the inherent instability of the UVES instrument.

5. Conclusions

We used a high-resolution spectral transit time series obtained with UVES to study the transmission spectrum of the hot Jupiter WASP-7 b, in particular the Na I D lines. We used telluric lines to account for instrumental drifts and carried out telluric correction using the molecfit package. To examine changes in the level of stellar magnetic activity, which might also affect the cores of

Table 5. Comparison of WASP-7 b parameters with those of other hot and ultra-hot Jupiters.

Planet	T_{eq} [K]	H^a [km]	ΔA^b [10^{-3}]	D_2 line contrast [%]	D_2 FWHM [\AA]	D_1 line contrast [%]	D_1 FWHM [\AA]	Refs. ^d
WASP-76 b	2160	1479	0.23	0.37 ± 0.09	0.61 ± 0.17	0.50 ± 0.08	0.68 ± 0.12	1, A
WASP-121 b	2358	1011	0.26	0.69 ± 0.12	0.73 ± 0.09	0.25 ± 0.09	0.9 ± 0.1	2, B
WASP-21 b	1333	951	0.25	$1.18^{+0.23}_{-0.24}$	$0.2^{+0.04}_{-0.03}$	$0.84^{+0.16}_{-0.17}$	0.31 ± 0.05	3, C
WASP-52 b	1315	672	0.4	1.31 ± 0.13	0.42 ± 0.03	1.09 ± 0.16	0.22 ± 0.03	4, D
WASP-7 b	1530	383	0.07	0.50 ± 0.06	0.13 ± 0.02	0.13 ± 0.04	0.13 ± 0.02	5, E
WASP-7 b (alt) ^c				0.49 ± 0.05	0.17 ± 0.02	0.19 ± 0.03	0.17 ± 0.02	5, E
MASCARA-2 b	2260	315	0.06	0.29 ± 0.04	0.16 ± 0.02	0.29 ± 0.04	0.15 ± 0.02	6, F
HD 189733 b	1140	200	0.11	0.64 ± 0.07	0.52 ± 0.08	0.40 ± 0.07	0.52 ± 0.08	7, G

Notes. (a) Atmospheric scale height. (b) Fraction of the stellar disk covered by an atmospheric annulus with a height of one scale height. (c) For WASP-7 b we show the result of the modeling by considering all spectra and by ignoring ten post-transit spectra (alt). (d) The numerals specify references for Na I D line contrasts and FWHMs, and letters denote references for the planetary effective temperature. We calculated the scale heights based on the references.

References. (1) Seidel et al. (2019); (A) West et al. (2016); (2) Cabot et al. (2020); (B) Delrez et al. (2016); (3) Chen et al. (2020a); (C) Ciceri et al. (2013); (4) Chen et al. (2020b); (D) Hébrard et al. (2013); (5) this work; (E) Southworth (2012); (6) Casasayas-Barris et al. (2019); (F) Talens et al. (2018); (7, G) Wyttenbach et al. (2015).

the Na I D line, we investigated the cores of the Ca II H and K, and hydrogen H α lines, which exhibit marginal evolution. In particular, no flaring or distinguishable rotational modulation was detected.

We carried out transmission spectroscopy of the Na I D lines, and accounted for the CLV and RM effects by means of simulations. The resulting transmission spectrum shows a narrow absorption feature at the wavelength of the Na I D₂ line, for which we determined a line contrast of 0.50 ± 0.06 % and a FWHM of 0.13 ± 0.02 Å, close to the instrumental resolution with a FWHM of 0.09 Å. Assuming the same width, we derived a line contrast of 0.13 ± 0.04 % for the Na I D₁ line. Disregarding ten post-transit spectra with lower S/N (exposures 70-80), we obtained line contrasts of 0.19 ± 0.03 % and 0.49 ± 0.05 % for the Na I D₁ and D₂ lines, respectively, with a FWHM of 0.17 ± 0.02 Å. Although consistent within the error, the so-determined line contrast of the Na I D₁ line is larger. We consider the detection for the Na I D₁ line absorption tentative, because the analysis of the BIC does not provide evidence for the presence of this line and, in our modeling, its width and shift are largely determined by the Na I D₂ line feature. Our investigation of the hydrogen Balmer lines (H α , H β , and H γ), the K I $\lambda 7699$ Å line, the Ca II H and K, and the IRT lines provided only upper limits for possible absorption features (Table 4).

Putting our results in the context of reports of Na I absorption in other systems, we find a good correlation between the fractional area of the stellar disk covered by an atmospheric annulus with a width of one scale height and the observed EWs of the Na I D₂ line features. Our results are consistent with this relation, as well as the empirical relation of Na I D₂ line strength described by Langeveld et al. (2022). Among the considered systems, those with stronger absorption signals tend to indicate primarily broader absorption and only moderately deeper lines in the transmission spectrum.

For reference, we calculated a synthetic Na I transmission spectrum using the pRT package, using an isothermal atmospheric model adapted to the WASP-7 system parameters. The model spectrum reproduced the observed line width well, but predicted overall weaker absorption. Both the pRT models, as well as observations in other systems such as MASCARA 2, also indicate significant absorption in the Na I D₁ line, compatible in strength with that in the D₂ line, which is hardly consistent with our results. While we show that the absorption signal in

the Na I D lines can plausibly be attributed to the planetary atmosphere, follow-up observations of WASP-7 b are required to clarify the situation in the Na I D lines and improve the precision of the measurement to further constrain the structure of the atmosphere.

Acknowledgements. We thank N. Casasayas-Barris and J. Seidel for their useful discussion. We thank F. Pfeifer for helping to take the observations. SC acknowledges support by DFG through project CZ 222/5-1. SK acknowledges financial support from the DFG through priority program SPP 1992 “Exploring the Diversity of Extrasolar Planets” (KH 472/3-1).

References

- Albrecht, S., Winn, J. N., Butler, R. P., et al. 2012, *ApJ*, 744, 189
 Barnes, J. R., Haswell, C. A., Staab, D., & Anglada-Escudé, G. 2016, *MNRAS*, 462, 1012
 Bonomo, A. S., Desidera, S., Benatti, S., et al. 2017, *A&A*, 602, A107
 Brown, T. M. 2001, *ApJ*, 553, 1006
 Cabot, S. H. C., Madhusudhan, N., Welbanks, L., Piette, A., & Gandhi, S. 2020, *MNRAS*, 494, 363
 Caccin, B., Cavallini, F., Ceppatelli, G., Righini, A., & Sambuco, A. M. 1985, *A&A*, 149, 357
 Casasayas-Barris, N., Pallé, E., Stangret, M., et al. 2021, *A&A*, 647, A26
 Casasayas-Barris, N., Pallé, E., Yan, F., et al. 2019, *A&A*, 628, A9
 Casasayas-Barris, N., Pallé, E., Yan, F., et al. 2020, *A&A*, 635, A206
 Castelli, F. & Kurucz, R. L. 2003, in *Modelling of Stellar Atmospheres*, ed. N. Piskunov, W. W. Weiss, & D. F. Gray, Vol. 210, A20
 Cauley, P. W., Kuckein, C., Redfield, S., et al. 2018, *AJ*, 156, 189
 Charbonneau, D., Brown, T. M., Noyes, R. W., & Gilliland, R. L. 2002, *ApJ*, 568, 377
 Chen, G., Casasayas-Barris, N., Pallé, E., et al. 2020a, *A&A*, 642, A54
 Chen, G., Casasayas-Barris, N., Pallé, E., et al. 2020b, *A&A*, 635, A171
 Ciceri, S., Mancini, L., Southworth, J., et al. 2013, *A&A*, 557, A30
 Czesla, S., Klocová, T., Khalafinejad, S., Wolter, U., & Schmitt, J. H. M. M. 2015, *A&A*, 582, A51
 Czesla, S., Mollé, T., & Schmitt, J. H. M. M. 2018, *A&A*, 609, A39
 Czesla, S., Schröter, S., Schneider, C. P., et al. 2019, *PyA: Python astronomy-related packages*, *Astrophysics Source Code Library*, record ascl:1906.010
 Czesla, S., Schröter, S., Wolter, U., et al. 2012, *A&A*, 539, A150
 Dekker, H., D’Odorico, S., Kaufer, A., Delabre, B., & Kotzlowski, H. 2000, in *Society of Photo-Optical Instrumentation Engineers (SPIE) Conference Series*, Vol. 4008, *Optical and IR Telescope Instrumentation and Detectors*, ed. M. Iye & A. F. Moorwood, 534–545
 Delrez, L., Santerne, A., Almenara, J. M., et al. 2016, *MNRAS*, 458, 4025
 Efron, B. & Stein, C. 1981, *The Annals of Statistics*, 9, 586
 Foreman-Mackey, D., Hogg, D. W., Lang, D., & Goodman, J. 2013, *PASP*, 125, 306
 Gaia Collaboration, Brown, A. G. A., Vallenari, A., et al. 2018, *A&A*, 616, A1
 Glidic, K., Schlawin, E., Wiser, L., et al. 2022, *AJ*, 164, 19
 Gray, D. F. & Brown, K. I. T. 2006, *PASP*, 118, 399

- Gray, R. O. & Corbally, C. J. 1994, *AJ*, 107, 742
- Hébrard, G., Collier Cameron, A., Brown, D. J. A., et al. 2013, *A&A*, 549, A134
- Hellier, C., Anderson, D. R., Gillon, M., et al. 2009, *ApJ*, 690, L89
- Kaltenegger, L. & Sasselov, D. 2011, *ApJ*, 736, L25
- Kass, R. E. & Raftery, A. E. 1995, *Journal of the American Statistical Association*, 90, 773
- Kausch, W., Noll, S., Smette, A., et al. 2015, *A&A*, 576, A78
- Khalafinejad, S., von Essen, C., Hoeijmakers, H. J., et al. 2017, *A&A*, 598, A131
- Klocová, T., Czesla, S., Khalafinejad, S., Wolter, U., & Schmitt, J. H. M. M. 2017, *A&A*, 607, A66
- Langeveld, A. B., Madhusudhan, N., & Cabot, S. H. C. 2022, *MNRAS*, 514, 5192
- Méndez, A. & Rivera-Valentín, E. G. 2017, *ApJ*, 837, L1
- Mollière, P., Wardenier, J. P., van Boekel, R., et al. 2019, *A&A*, 627, A67
- Nikolov, N., Sing, D. K., Fortney, J. J., et al. 2018, *Nature*, 557, 526
- Oshagh, M., Santos, N. C., Ehrenreich, D., et al. 2014, *A&A*, 568, A99
- Redfield, S., Endl, M., Cochran, W. D., & Koesterke, L. 2008, *ApJ*, 673, L87
- Salz, M., Czesla, S., Schneider, P. C., et al. 2018, *A&A*, 620, A97
- Schwarz, G. 1978, *Ann. Statist.*, 6, 461
- Seager, S. & Sasselov, D. D. 2000, *ApJ*, 537, 916
- Seidel, J. V., Ehrenreich, D., Wyttenbach, A., et al. 2019, *A&A*, 623, A166
- Serrano, L. M., Oshagh, M., Cegla, H. M., et al. 2020, *MNRAS*, 493, 5928
- Smette, A., Sana, H., Noll, S., et al. 2015, *A&A*, 576, A77
- Snellen, I. A. G., Albrecht, S., de Mooij, E. J. W., & Le Poole, R. S. 2008, *A&A*, 487, 357
- Southworth, J. 2012, *MNRAS*, 426, 1291
- Southworth, J., Dominik, M., Jørgensen, U. G., et al. 2011, *A&A*, 527, A8
- Talens, G. J. J., Justesen, A. B., Albrecht, S., et al. 2018, *A&A*, 612, A57
- Virtanen, P., Gommers, R., Oliphant, T. E., et al. 2020, *Nature Methods*, 17, 261
- Vogt, S. S., Penrod, G. D., & Hatzes, A. P. 1987, *ApJ*, 321, 496
- West, R. G., Hellier, C., Almenara, J. M., et al. 2016, *A&A*, 585, A126
- Wyttenbach, A., Ehrenreich, D., Lovis, C., Udry, S., & Pepe, F. 2015, *A&A*, 577, A62
- Wyttenbach, A., Lovis, C., Ehrenreich, D., et al. 2017, *A&A*, 602, A36
- Yan, F., Fosbury, R. A. E., Petr-Gotzens, M. G., Zhao, G., & Pallé, E. 2015, *A&A*, 574, A94
- Zhang, Y., Snellen, I. A. G., Wyttenbach, A., et al. 2022, *arXiv e-prints*, arXiv:2208.11427

Appendix A: Best-fit parameters and transmission spectra

We carried out the same analysis as mentioned in Sect. 3.5, and derived the result of the best-fit parameters and the transmission spectrum of Na I D lines by ignoring ten post-transit spectra (exposure 70-80). In addition, we obtained the transmission spectra of WASP-7 b for other lines, as described in Sect. 3.7.

Table A.1. Best-fit parameters along with 68 % credibility intervals of the transmission spectrum model 2.

Parameter	Value	Unit
$P0$	0.0084 ± 0.0039	
$P1$	0.0009 ± 0.0003	\AA^{-1}
s	0.491 ± 0.050	
RV	0.836 ± 0.591	$[\text{km s}^{-1}]$
Contrast D_2	0.495 ± 0.056	$[\%]$
Contrast D_1	0.191 ± 0.039	$[\%]$
FWHM	0.17 ± 0.02	$[\text{\AA}]$
Model	k	BIC
No s	6	1434.4
No Abs	3	1536.1
Only D_2	6	1378.1
Only D_1	6	1533.3
D_1 and D_2	7	1359.0

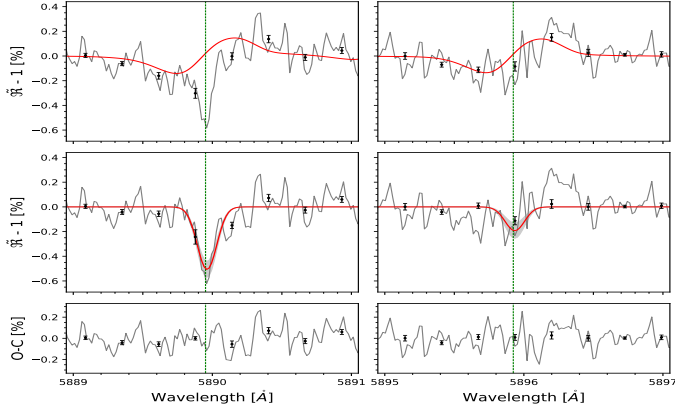


Fig. A.1. Transmission spectrum of WASP-7 b around the Na I D_2 (left column) and Na I D_1 line (right column) by disregarding ten post-transit spectra. Top panels: Observed transmission spectrum (gray) along with best-fit model components, representing the CLV and RM effects (solid red). Middle panels: Observed transmission spectrum with the best-fit Gaussian absorption components (red), and with the model shown in the upper panels subtracted (gray). The gray shades denote 1σ uncertainty of the best-fit model (red). Bottom panel: Residuals with respect to the best-fit model. The black data points correspond to binning by a factor of 15.

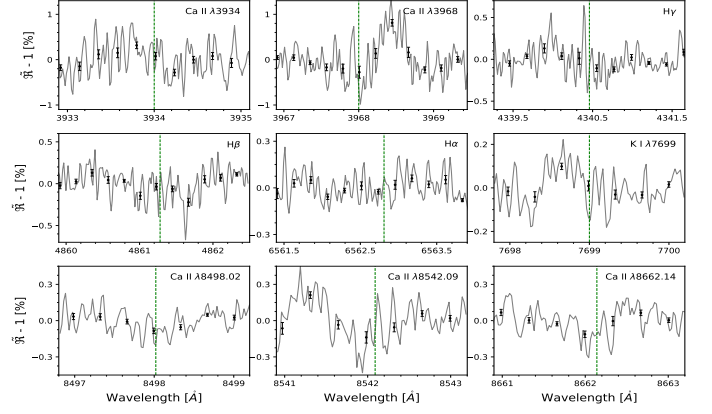


Fig. A.2. Observed transmission spectra of WASP-7 b for other lines (gray). Black data points correspond to binning by a factor of 15 and dashed vertical green lines indicate the centers of the lines.